



HAL
open science

Neural network model for atmospheric attenuation retrieval between 20 and 50 GHz by means of dual-frequency microwave radiometers

Laurent Barthès, Cécile Mallet, Peter Golé

► **To cite this version:**

Laurent Barthès, Cécile Mallet, Peter Golé. Neural network model for atmospheric attenuation retrieval between 20 and 50 GHz by means of dual-frequency microwave radiometers. *Radio Science*, 2003, 38 (5), pp.1082. 10.1029/2002RS002813 . insu-02183221

HAL Id: insu-02183221

<https://insu.hal.science/insu-02183221>

Submitted on 15 Jul 2019

HAL is a multi-disciplinary open access archive for the deposit and dissemination of scientific research documents, whether they are published or not. The documents may come from teaching and research institutions in France or abroad, or from public or private research centers.

L'archive ouverte pluridisciplinaire **HAL**, est destinée au dépôt et à la diffusion de documents scientifiques de niveau recherche, publiés ou non, émanant des établissements d'enseignement et de recherche français ou étrangers, des laboratoires publics ou privés.

Neural network model for atmospheric attenuation retrieval between 20 and 50 GHz by means of dual-frequency microwave radiometers

Laurent Barthes, Cécile Mallet, and Peter Gole

Centre d'Etude des Environnements Terrestres et Planétaires (CETP), Vélizy, France

Received 7 November 2002; revised 23 May 2003; accepted 20 June 2003; published 17 September 2003.

[1] The propagation of signals through the atmosphere plays a major role in the quality of communications between ground terminals and satellites. Its characteristics have to be known accurately for appropriate communications equipment to be selected. In the band of frequencies used by operators in the future generation of satellites (beyond 20 GHz), the quality of transmission is especially affected by the attenuation of received signals because of rain, and by other less significant but much more frequent effects due to atmospheric gases, and nonprecipitating water. These phenomena have a direct impact on the availability ratio of a link between a ground terminal and a satellite. Our main goal in this study is to measure the atmospheric attenuation, using dual-frequency ground-based radiometers measuring the sky radiation at different pointing directions, so as to perform a statistical study. A new algorithm, based on a neural approach, is thus developed for estimating atmospheric attenuation, in various meteorological conditions, for several elevation angles and for frequencies between 20 and 50 GHz, from dual-frequency radiometric measurements. A validation of the obtained algorithm is performed on Olympus experimental data for the 20 and 30 GHz channels. At the end of this paper some applications are then presented to underline the usefulness of this new algorithm. The applicability of the algorithm to satellite beacon calibration in Ka or Q band with accuracy of 0.1 dB is shown. Preliminary joint statistics between attenuation at various pointing directions obtained at 40 GHz show what improvement can be expected from satellite diversity in the case of satellite constellations. *INDEX TERMS*: 6904 Radio Science: Atmospheric propagation; 3359 Meteorology and Atmospheric Dynamics: Radiative processes; 3354 Meteorology and Atmospheric Dynamics: Precipitation (1854); 3360 Meteorology and Atmospheric Dynamics: Remote sensing; *KEYWORDS*: atmospheric attenuation, neural networks, propagation

Citation: Barthes, L., C. Mallet, and P. Gole, Neural network model for atmospheric attenuation retrieval between 20 and 50 GHz by means of dual-frequency microwave radiometers, *Radio Sci.*, 38(5), 1082, doi:10.1029/2002RS002813, 2003.

1. Introduction

1.1. Context

[2] The operators of communications satellites plan to use frequency bands higher than 20 GHz. The development of algorithms to allow the statistical study of atmospheric attenuation at these frequencies using a ground-based experimental device is thus of great interest. The main areas of application of propagation research at frequencies between 20 and 50 GHz are fixed, and mobile, satellite communications system.

[3] Characteristics of atmospheric attenuation in the frequency band of interest to this paper are two-fold. On the one hand, atmospheric attenuation can cause a significant degradation of the received signal (very large attenuations are observed that can lead to signal loss during severe storms). On the other hand, it shows a very large spatial heterogeneity, especially with regard to rain. Therefore, the effective use of this part of the spectrum is possible only by implementing techniques to mitigate atmospheric fading (up link power control, modulation or adaptive coding and diversity).

[4] In the case of fixed satellites, the frequencies used for IP-over-satellite and video-on-demand are primarily Ku-band (12–14 GHz). Growing demand coupled with

the need for growing bandwidth makes the use of Ka-band (20–30 GHz) unavoidable for multimedia satellite services. The next step is to move to higher frequencies such as Q-band (36–46 GHz). Propagation studies at these frequencies are thus needed [Arbesser-Rastburg, 2002]. This study makes it possible to characterize the statistical behavior of the channel as a function of frequency and elevation angle from the attenuation point of view.

[5] For Ka-band mobile satellite communication systems, satellite constellations are subjected to atmospheric attenuation, which is very inhomogeneous, especially in the presence of rain or clouds. Using a technique known as satellite diversity may solve this problem. The last part of the present paper aims at quantifying the improvement in terms of availability of a link if at least two satellites are simultaneously visible from the same place, that is, if the satellites of the constellation are numerous enough.

[6] In the near future satellite experiment will be necessary for the exploration of Ka and Q band satellite communication. The work presented in this paper, among other things, aims at developing an algorithm for satellite beacons calibration using brightness temperatures measured by dual-frequency radiometers.

1.2. Objectives and Methodology

[7] Our main goal is to determine the atmospheric attenuation, in several directions, for frequencies between 20 and 50 GHz from radiometer brightness temperatures measured at 20 and 30 GHz. Some Experiments performed previously (OLYMPUS, ITALSAT) [Polonio and Riva, 1998] or to be performed (SYRACUSE 3) allow the attenuation of a link between a ground station and a satellite to be directly estimated. They require beacons on board the satellite so that at the present time this kind of measurement remains relatively scarce. Moreover, for the study of satellite diversity, two or several satellites would be necessary, thus increasing the cost of the experiment.

[8] A more economic solution is proposed in this paper, which consists in using two dual-frequency ground-based radiometers measuring the sky radiation at different pointing directions. The experiment, located on the experimental site of Institut Pierre Simon Laplace (near Paris), comprises two radiometers placed side by side, associated with an additional spectropluviometer, and other sensors (atmospheric pressure at ground level, temperature). Sky brightness temperature measurements are obtained at 23.8 and 31.7 GHz with a RESCOM radiometer, for zenith angles between 0 and 60°, and at 23.8 and 36.5 GHz with the DRAKKAR radiometer. Both are balanced Dicke radiometer. An integration time of 1 s leads to a resolution of 0.3 K, and a accuracy of 1.5K is obtained by using tip-curve calibration. For each radiometer, one channel is

sensitive to water vapor absorption and the other to liquid water absorption. Brightness temperatures are then converted by means of the statistical model that has been developed and validated as described below, into atmospheric attenuation at various frequencies ranging from 20 to 50 GHz. As explained later, the main limitation of our approach is the difficulty to estimate larger attenuations by means of ground-based radiometers. A validation of the obtained results by a comparison with attenuations measured during the Olympus experiment allows this limitation to be quantified.

[9] After some general considerations pertaining to atmospheric attenuation (section 2) and the retrieval algorithm using radiometric measurements (section 3), this paper describes a new statistical neural-network model for estimating the attenuation undergone by a radio link between a terminal on the ground and a satellite. The simulated database used to develop this neural network algorithm is described in section 4. Section 5 shows the performance of this new algorithm at the 20 and 30 GHz using Olympus experimental data. In the last part of this paper, applications of the algorithm to carry out attenuation measurement campaigns are presented.

2. Atmospheric Attenuation

[10] In the microwave range, between 10 and 60 GHz, atmospheric absorption is due to atmospheric gases and hydrometeors [Ulaby *et al.*, 1981]. In the Earth's atmosphere, oxygen and water vapor are the only constituents that exhibit significant absorption bands in the microwave spectrum [Liebe *et al.*, 1993; Rosenkranz, 1998]. In the microwave region, water vapor has rotational absorption lines at 22.235 and 183.31 GHz. The microwave absorption spectrum of oxygen consists of a large number of absorption lines between 50 and 70 GHz and an additional line at 118.74 GHz.

[11] The total gaseous absorption coefficient k_g at height z for a frequency f , is thus given by

$$k_g(f, z) = k_{H_2O}(f, z) + k_{O_2}(f, z) [Npkm^{-1}]. \quad (1)$$

For a given frequency, this coefficient depends on temperature, pressure, and relative humidity, of the atmosphere at height z .

[12] The interaction of electromagnetic radiation with particles (such as those in clouds, fog, snow, or rain) may involve both absorption and scattering. The volume extinction coefficient is governed by the density, shape, size distribution, and dielectric properties of the particles contained in the volume.

[13] Clouds, on the other hand do not contain particles with radii greater than 0.1 mm, so that the Rayleigh

approximation is applicable at the considered frequencies considered here [Ulaby *et al.*, 1981]. For ice particles, the imaginary part of the refractive index of ice is very small. The attenuation due to ice clouds is thus negligible relative to water clouds.

[14] Because raindrops are larger than drops in clouds, ignoring scattering effects of rain in favor of absorption is valid only over a limited combined range of rain rates and frequencies. Thus, scattering effects are taken into account in the simulation that has been performed here (see section 4.2). However, for simplicity, scattering effects are not taken into account in the following equation. The extinction coefficients for clouds (k_c) and rain (k_r) are equal to volume absorption coefficients and for a given frequency they depend only on water content and temperature at height z .

[15] The total absorption coefficient at height z thus consists of contributions due to atmospheric gases, clouds and precipitation. It is given by

$$k_a(f, z) = k_g(f, z) + k_c(f, z) + k_r(f, z) \quad [Npkm^{-1}]. \quad (2)$$

For a zenith angle θ smaller than 70° , a spherically stratified atmosphere may be approximated by a planar atmosphere. Thus, the optical depth τ of the atmosphere between 0 and z is given by

$$\tau(f, z, \theta) = \sec(\theta) \int_0^z k_a(f, u) du \quad [Np]. \quad (3)$$

The atmospheric transmissivity for the entire atmosphere is defined by

$$t(f, \theta) = \exp(-\tau(f, \infty, \theta)). \quad (4)$$

When expressed in dB, the total atmospheric loss factor $1/t(f, \theta)$, becomes $A(f, \theta)$, and is referred to as the atmospheric attenuation.

$$A(f, \theta) = 4.343\tau(f, \infty, \theta) \quad [dB]. \quad (5)$$

In fact, under clear-sky conditions (k_a equals k_g), the atmospheric attenuation is relatively small (except for $50 < f < 70$ GHz), and the involved absorbing constituents (gases) are more or less horizontally stratified. On the contrary, in the presence of clouds and even more so in the presence in rain, the increase in atmospheric attenuation is combined with an increase in its horizontal variability. The statistical study of atmospheric attenuations simultaneously measured at various elevation angles will show the interest of the satellite diversity technique. In the last part of this paper a statistical study of attenuation for various pointing directions simultaneously visible from a given point on

the ground is performed. Our aim is to check whether the correlation between various pointing directions is sufficiently small to make the technique of satellite diversity valuable for frequencies between 20 and 50 GHz. In other words, by assuming that higher attenuation values can be observed usually in a highly heterogeneous atmosphere, the angular distance between two different links, for which they are not both simultaneously affected by rain, will be estimated.

3. Attenuation Retrieval by Means of a Radiometer

3.1. Brightness Temperature

[16] The basic principle of radiometry is that a fixed relation exists between the absorption of a medium and its spontaneous emission of thermal radiation. A radiometer is a passive receiver, which measures, in a given direction, the electromagnetic energy radiated by the medium. In our case, each component of the atmosphere (gases, hydrometeors) will contribute some of this radiation, to which it will be necessary to add the cosmic radiation background. For a nonscattering atmosphere, the sky brightness temperature measured at the ground surface is given by the radiative transfer equation [Chandrasekhar, 1960]

$$T_B(f, \theta) = T_c t(f, \theta) + \sec(\theta) \int_0^\infty T(z) \exp(-\tau(f, z, \theta)) \cdot k_a(f, z) dz \quad [K], \quad (6)$$

where $T(z)$ is the physical temperature at height z and T_c is the cosmic background.

[17] The above formulas show that attenuation and brightness temperature depend on the same atmospheric parameters (temperature, pressure, water vapor, cloud liquid water and precipitation profiles). In the presence of rain, scattering effects have to be added in the radiative transfer equation, as explained in section 4.2.

[18] The main limitation of this approach, which consists in using radiometers to measure atmospheric attenuation, is that large values of attenuation cannot be correctly estimated for two reasons:

[19] First, large attenuations are predominantly caused by rain, so that the water films and flows occurring on the radiometer reflectors modify their reflection coefficient, thus making the radiometer measurement erroneous. For this reason, blowers have been added to the radiometers used in the present experiment to allow measurements to be carried out during small rain events and immediately after rain events.

[20] Second, because of a saturation phenomenon: if the atmospheric optical depth $\tau(\theta)$ increases, the electro-

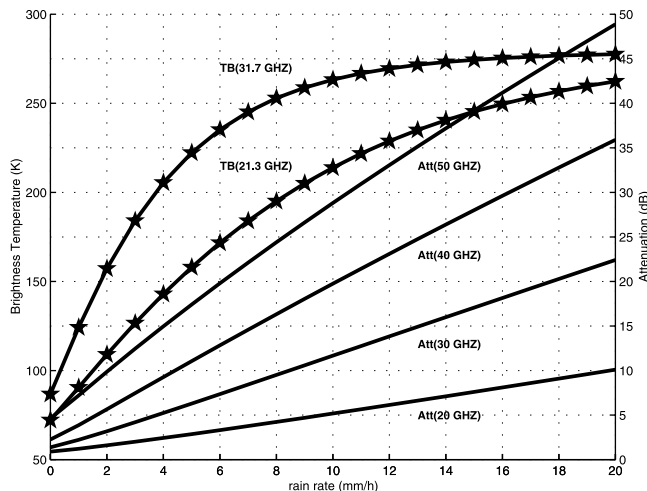


Figure 1. Brightness temperature of the sky and attenuation for frequencies between 20 and 50 GHz, and zenith angle of 60° , as a function of rain rate.

magnetic radiation due to the upper atmospheric layers are strongly attenuated by the lower layers, so that the radiometer mainly receives radiation originating from the lower part of the atmosphere. Figure 1 shows the variation of brightness temperature at 21 and 36 GHz and atmospheric attenuations estimated at 20, 30, 40 and 50 GHz for a homogeneous rain layer at different rain rates. These curves were all obtained for the same pointing direction, namely, a zenith angle θ of 60° . The higher the rain rate of the layer, the smaller the brightness temperature increase, whereas the attenuation continues to increase regularly. For high brightness temperatures, this saturation phenomenon, combined with the effect of measurement uncertainty, leads to an increase in the uncertainty of attenuation retrieval. Even in the absence of rain or thick clouds, a previous study [Bosisio and Mallet, 1998] had underlined the nonlinearity of the relationship between brightness temperature and integrated atmospheric contents.

3.2. Existing Models for Small Attenuations

[21] These models have been developed and used to estimate the attenuation due to the atmosphere with a very high precision (0.1 dB), but only in periods of clear sky.

3.2.1. Classical Approach

[22] The effective temperature, T_m , which is a profile- and frequency- dependent quantity, is defined as

$$T_m(f) = \frac{\sec(\theta)}{1 - t(f, \theta)} \int_0^\infty T(z) \exp(-\tau(f, z, \theta)) \cdot k_a(f, z) dz \quad [K]. \quad (7)$$

Using this quantity and the radiative transfer equation (6), the total attenuation (5) can also be written as

$$A(f, \theta) = 10 \log \left(\frac{T_m(f) - T_c}{T_m(f) - T_B(f, \theta)} \right) \quad [dB]. \quad (8)$$

This model assumes that T_m is known. It is generally considered to be constant (280 K). This model is accurate only for very small attenuations that correspond to the clear-sky condition (i.e., when $T_B \ll T_m$). As shown in Figure 2, this assumption is not valid when it is desired to increase the validity range of the model to cloudy or slightly rainy situations. This has been confirmed by the fact that the effective temperatures T_m computed for various meteorological conditions provided by the European Centre for Medium-Range Weather Forecasts (ECMWF), see section 4.1 for more details, shows a great variability depending on the climatic zones.

3.2.2. C.N.E.T Model

[23] This model [Mallet and Lavergnat, 1992] was developed in the context of the *Olympus Propagation Experiment (OPEX)* [1994]. It was used to calibrate the measurements, of the OLYMPUS 20 and 30 GHz beacon, carried out with the French ground station, and had been specifically developed for estimating the attenuation in periods of clear sky with an accuracy of 0.1 dB:

$$t(f, \theta) = \alpha(f, \theta) * T_{B_{21}} + \beta(f, \theta) T_{B_{31}} + \gamma(f, \theta). \quad (9)$$

This model assumes a linear relation between atmospheric transmissivity and the two brightness temperatures (in kelvins) at 21.3 and 31.7. The atmospheric attenuation is thus derived using equations (4) and (5).

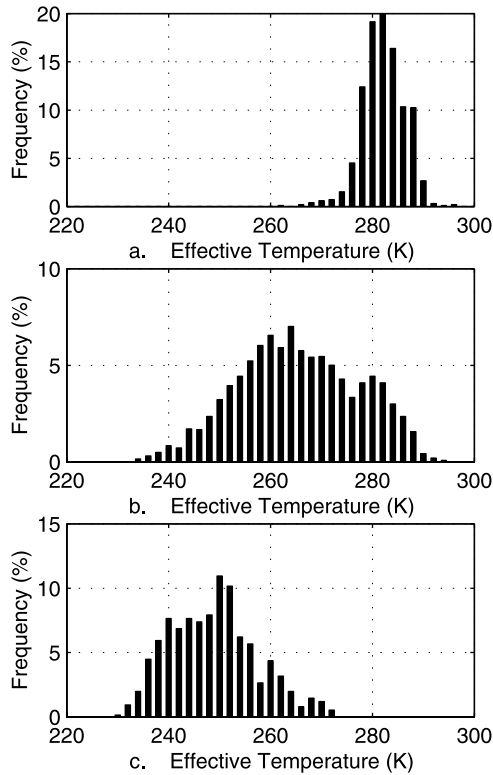


Figure 2. Distribution of effective temperature T_m at 20 GHz for different climatic areas: (a) the equator, (b) medium latitudes, and (c) poles.

Sets of coefficients (α , β , γ) were determined for various frequencies and elevation angles of the satellite. Because of the lack of radiometer measurements collocated with atmospheric soundings, simulated databases have been used to obtain these coefficients. A large set of vertical profiles (of pressure, temperature, humidity) obtained from radiosoundings, have been associated with 14 standard cloud models. A radiative transfer model able to simulate brightness in clear or cloudy conditions has been used to build a sufficiently large database. However, this linear model is no longer applicable for the present study because its validity range is restricted to small attenuations, between 0 and 1 dB at 20 GHz, since it was developed specifically for beacon calibration, in order to retrieve clear-sky attenuation.

3.3. A New Approach

[24] The aim here is to extend this previous model so as to estimate atmospheric attenuation at a given frequency f and a given zenith angle θ from two measured brightness temperatures. Similarly to the previous model, the output of the new algorithm is transmissivity, the atmospheric attenuation being computed according to

equations (4) and (5). Now, the problem to be solved is to derive a law of the following form:

$$t(f, \theta) = F[T_{B_1}(\theta), T_{B_2}(\theta), \sec(\theta), f], \quad (10)$$

where f ranges from 20 to 50 GHz, and θ , from 0° to 60° .

[25] The inputs $T_{B_1}(\theta)$ and $T_{B_2}(\theta)$ are a pair of brightness temperatures measured at frequencies f_1 and f_2 for a zenith angle of θ . Frequency f_1 is within the water vapor absorption line (near 22 GHz) and frequency f_2 is located between the water vapor and oxygen absorption lines (between 30 and 40 GHz); thus one channel is sensitive to the water vapor contribution and the other, to the liquid water contribution. The frequency pairs considered in this paper are given in section 1.2. The zenith angle θ corresponding to the measurement direction and the frequency f at which the attenuation had to be estimated are also inputs to the new model so as to avoid an interpolation, which would otherwise be needed when the model coefficients are computed only for a finite number of angles and frequencies. The atmospheric transmissivity depends on the atmospheric thickness, so that the cosecant of the zenith angle is used as an input. A possible improvement by using other parameters, such as ground pressure or temperature, has also been tested, but has not proved to be significant for $f < 50$ GHz and thus, will not be reported here.

[26] As explained above, the linear assumption used in the previous model is no longer valid in case of heavy clouds [Bosisio and Mallet, 1998] or rain. It is indeed advisable to take into account the saturation effect on the measurement of the brightness temperatures by introducing a nonlinearity into the model. For this reason, we chose to use an artificial neural network (NN) approach whose ability to model nonlinearity is well known [Haykin, 1999]. However, this approach, like most statistical methods, is particularly sensitive to the statistical representativeness of the database used for the development. The two following paragraphs are devoted to the development of this new algorithm, while the next part describes how the data are simulated and is followed by a description of the new model itself.

4. Simulated Database

[27] As explained in the next section, NNs must be trained to process inputs before they can be used in a given application. This training is performed in a supervised manner and involves the development of a training base. Thus, a very large database containing the NN input data ($T_{B_1}(\theta)$, $T_{B_2}(\theta)$, $\sec(\theta)$, f) and corresponding targets ($t(f, \theta)$) is generated. The scarcity of in situ meteorological data concerning cloud systems implies tackling this problem through simulated data. It is thus a matter of computing, for many different meteorological

situations, on the one hand the ground-based radiometer measurements, and on the other hand, the quantities to be retrieved (attenuations or transmissivity).

4.1. Selected Atmospheric Profiles

[28] The atmospheric profiles are obtained from the European Centre for Medium-Range Weather Forecasts (ECMWF) model [Tiedtke, 1993]. Initially, 42,000 data points were available, corresponding to the 36-hour forecast experiment performed on 10 and 16 February 1998. Each data item consists in profiles of temperature, pressure, moisture, cloudy liquid water, cloud cover, precipitation rain and ice, for 31 altitude levels with a spatial resolution of $0.5^\circ \times 0.5^\circ$.

[29] The variety of situations is ensured by the global geographic coverage. In fact, a previous study [Gérard and Eymard, 1998] has shown that even if only a few days are considered, the global coverage is representative of the natural seasonal variability of the atmospheric parameters. A specific processing is performed in order to obtain a statistically representative subset. This reduction in the number of samples is imposed because of the large computing time involved and also because of the natural distribution of meteorological situations. As can be expected smaller, atmospheric attenuations correspond to the most frequently occurring meteorological situations. Therefore, a NN trained on such a data set will only be able to correctly learn the relation (10) that corresponds to weak attenuation. The problem to be solved is to reduce the number of data only in areas of large probability density, while preserving the least frequent cases. The difficulty in this selection resides in the dimension of the data space. In fact, each data item consists in seven atmospheric profiles with 31 vertical layers, so that the initial data space dimension is greater than 200. A reduction in this dimension is first done by extracting 13 quantities characteristic of each data item (such as water vapor integrated content, cloud liquid water content, rain rate, ground temperature and pressure, ...). A selection is then performed by using a representation of the whole data set with a Self-Organizing Map (SOM). Algorithms proposed by Kohonen [2001] have been used to obtain such a map. As explained by Haykin [1999] in a book devoted to neural networks, a SOM has three properties: (1) The SOM algorithm is able to represent a large set of input data by finding a smaller set (a map) of prototypes (neurons), so as to provide a good approximation of the original input space. (2) The computed map is topologically ordered, that is, the spatial location of each neuron corresponds to a particular domain or feature of the input data. (3) The obtained map reflects the variation in the statistics of the input distribution; in other words, SOM map is able to approximate the probability distribution function of the input data set.

[30] SOM maps may thus be viewed as a nonlinear generalization of the principal component analysis. In our case a 2-D map of 23×23 neurons has been generated. Each of the 529 neurons corresponds to a cluster of neighbor profiles in the input space. The number of profiles retained in each cluster depends on the density of the considered cluster. Finally, 5268 profiles were retained. The aim of this selection is double: to keep the maximum variety of atmospheric profiles, and the need to over-represent rare cases so as to be able to develop neural network algorithms capable of retrieving attenuation in a large range of values.

4.2. Radiative Transfer Model Used to Construct the Databases

[31] A radiative transfer model [Moreau et al., 1999] applied to the selected profiles allowed the construction of a large simulated database. This model determines the radiative transfer of radiation through a horizontally stratified atmosphere, also referred to as a one-dimensional plane-parallel model. It uses the discrete ordinate eigenanalysis method [Tsang et al., 1985] to solve the radiative transfer equation. Concerning the absorption of gases (oxygen and water vapor), Liebe's Microwave Propagation Model [Liebe et al., 1993] was selected in accordance with the results of English et al. [1994] for computing the atmospheric attenuation. For frequencies below 60 GHz, the scattering effect of clouds is negligible, so that the cloud liquid water is considered as being comprised of Rayleigh particles. For rain, the particles are thus assumed to be spherical and the components of the scattering matrix are computed using Mie's theory, with the Marshall and Palmer [1948] law for the particle size distribution. A noise, uniformly distributed between -1.5 K and $+1.5$ K, was added to simulated brightness temperatures; this corresponds to measurement uncertainty.

[32] For each of the 5268 selected profiles the brightness temperatures (6) at radiometer frequencies f_1 and f_2 and the transmissivity (4) are computed for 27 different values of frequency ($f = 18.5, 20, 20.7, 21.3, 22.5, 23.8, 25, 26, 27, 28, 29, 30, 31.7, 32, 33.5, 35, 36.5, 37, 38, 39, 40, 41.4, 43, 45, 47, 50$ and 51 GHz) and 9 zenith angles ($\theta = 0^\circ, 30^\circ, 50^\circ, 52.7^\circ, 55^\circ, 52.7^\circ, 55^\circ, 57.7^\circ$ and 60°) so as to obtain cosecant values that are approximately regularly spaced. Finally, a set of $27 \times 9 \times 5268 = 1280124$ triplets (brightness temperature at f_1 and f_2 frequencies, and transmissivity) is thus computed.

5. Algorithm for Attenuation Measurement

5.1. Training of Neuronal Model (MLP)

[33] Several theoretical results prove the usefulness of NNs as a universal approximator [Cibenko, 1989; Hornik

et al., 1989]. NNs are capable of learning from examples and do not require a priori assumptions about the function that they approximate. However, theory shows the existence of an architecture, but it does not indicate how to choose it.

[34] The neural network used to model the relationship given in (10) is a Multi-Layered Perceptron (MLP). A neuron is a nonlinear, parametric and bounded, algebraic function. A MLP applies an algebraic function to its inputs, by combining the functions performed by each of its neurons. A neuron is defined by its state o_i , its connection weights w_{ij} to neurons located upstream, and its activation function f . It carries out following operation:

$$o_i = f(s_i) \quad \text{with} \quad s_i = \sum_{j=1}^n w_{ij} o_j. \quad (11)$$

The use of nonlinear activation functions f makes it possible to obtain nonlinear statistical models.

[35] A NN is defined by its architecture and weights. In other words, it is characterized by its topology, namely, the number of inputs, outputs and hidden neurons, the chosen activation function f , and how neurons are interconnected. A MLP consists of successive layers (a layer is a set of nonconnected neurons). All connections are directed from lower to upper layers. Neurons of the first hidden layer derive their state from the inputs of the model with their assigned weights. Neurons of other layers derive their state from the outputs of the previous layer with their own weights.

[36] For a fixed architecture, the set of functions defined by the network depends on set of weights W of its various connections. A particular architecture thus generates a family of functions:

$$\begin{aligned} \mathfrak{R}^p &\rightarrow \mathfrak{R}^q \\ x &\rightarrow y = F(W, x). \end{aligned} \quad (12)$$

The estimation of the weights, which constitutes the learning process, requires a wide set, D , of input/output pairs corresponding to the system to be modeled by the NN. In our case,

$$\begin{aligned} D &= \{(x_i, y_i), i = 1 \dots N\} \\ \text{where} \begin{cases} x = [T_{B_1}(\theta), T_{B_2}(\theta), \sec(\theta), f] \\ y = t(\theta, f). \end{cases} \end{aligned} \quad (13)$$

The optimal architecture obtained is described in Figure 3. Finally, two different neural networks with the same architecture (two hidden layers of 18 neurons each) were trained. So as to obtain two different sets of weights: A first neural network has been trained on frequencies between 18 and 25 GHz and the second one

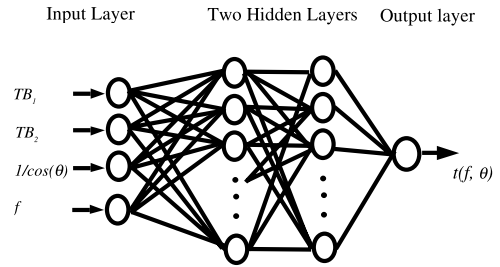


Figure 3. Architecture of the neural network developed. Four inputs: a pair of brightness temperatures TB at two different frequencies f_1 and f_2 , the cosecant of zenith angle θ and the frequency (f). One output: the atmospheric transmissivity at frequency f and zenith angle θ .

on frequencies between 25 and 50 GHz. In fact due to gaseous absorption we observe a high nonlinearity near the 22.5 GHz water vapor line and above 40 GHz (oxygen absorption lines). This separation in to two different frequency ranges provides better performance than a global network.

[37] The learning step consists in determining the weights W by minimizing a cost function, i.e., a measure of the mismatch between target values and predicted values. The expression of this empirical cost function $J(W)$ is the following least squares error function:

$$J(W) = \sum_{i=1}^N (y_i - F(W, x_i))^2. \quad (14)$$

To approach the minimum of this multidimensional cost function, a gradient technique, which is an iterative optimization method, adapted to MLP by gradient back-propagation [Bishop, 1995], is used. Cross-validation tests, based on a procedure referred to as the early stopping method of training [Haykin, 1999], allowed us to control the quality of the minimum estimation and of generalization. Theory shows that, if the architecture of the MLP is well chosen, the minimization of $J(W)$ is achieved correctly, and the observation set is consistent with the true field of variables, the MLP giving an accurate approximation of the mean fields of the variable y . Specifically:

$$F(x, W) \approx E[Y/x].$$

In the present case, $E[Y/x]$ is the conditional average of transmissivity. This allows one to fit the desired nonlinear transfer function using noisy data.

5.2. Generalization on Simulated Data

[38] In the following, the performance of the model is obtained in a general case on a subset of data that was

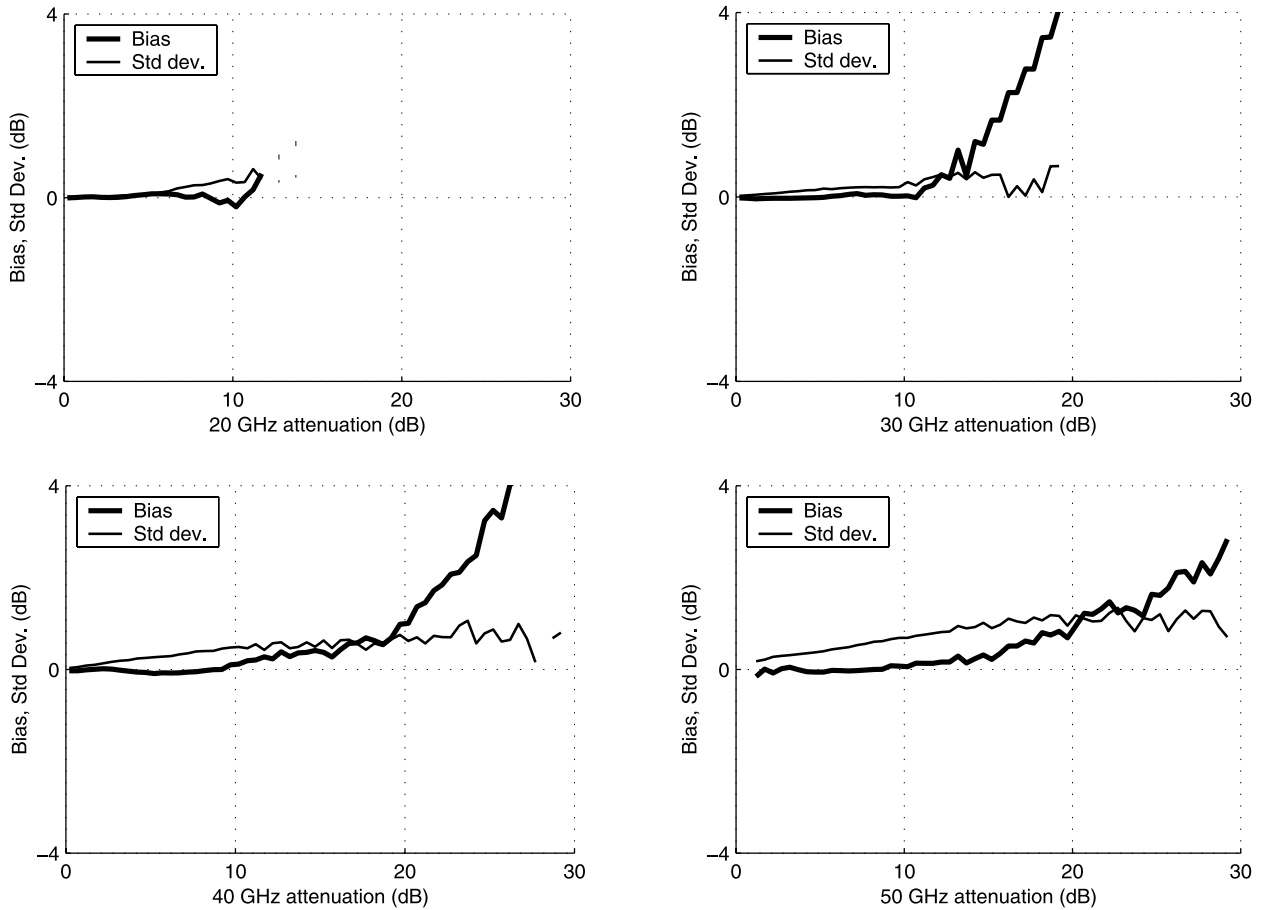


Figure 4. Generalization error of the NN attenuation model at 20, 30, 40 and 50 GHz obtained on simulated data. The thick line corresponds to the error bias, and the thin line corresponds to the standard deviation error as a function of attenuation.

not used during the learning step, the test set. The quality of the obtained model is considered with respect to the statistical and physical results it leads to. Figure 4 shows the evolution of the bias and standard deviation of the error function of attenuation obtained for 20, 30, 40 and 50 GHz, respectively, for all considered zenith angles. It should be noted that error increases with increasing attenuation, either due to atmospheric content or length of atmospheric path (zenith angle). For a 20 GHz attenuation lower than 7 dB and a 40 GHz attenuation lower than 15 dB results are reasonable. This corresponds to clear or cloudy sky conditions as well as to some rainy events. The higher the zenith angle, the more likely these limits will be reached for small rain rates because of the saturation phenomena described in section 3.1.

[39] So as to check whether the neural network correctly models the underlying physics, we have verified

for numerous profiles that the relation between the radiometer measurements and the atmospheric transmissivity at different frequencies and different angles was well represented by the networks. Figure 5 shows the attenuation versus frequency for two different zenith angles ($\theta = 0^\circ$ and 60°) and for two particular samples corresponding to small (Figure 5a) and large (Figure 5b) attenuation situations, respectively.

[40] Solid curves are those given by the statistical model (new NN algorithm) and the curves marked with circles by the physical one (radiative transfer model described in section 4.2). As can be seen, the non-linearity of the relation between measurements and transmissivity is well represented by the networks. The gaseous absorptions are correctly estimated for frequencies below 45 GHz as evidenced by the presence of the water vapor and oxygen absorption lines in Figure 5a. For frequencies in the neighborhood of the oxygen

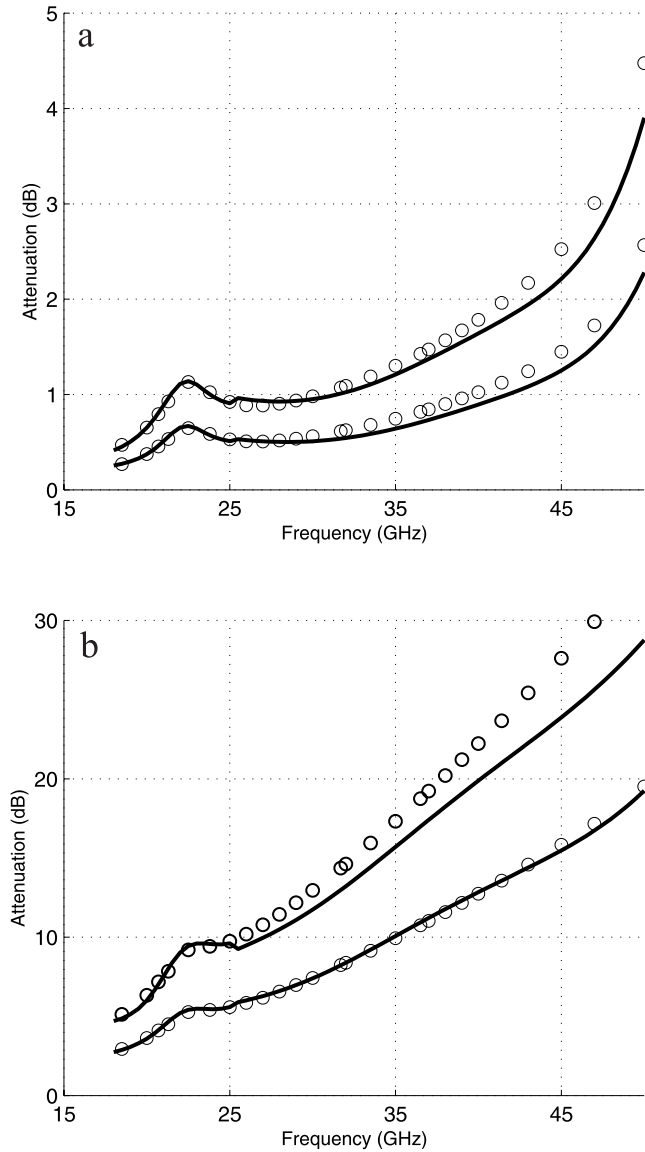


Figure 5. Attenuation versus frequency obtained for two particular atmospheric profiles corresponding to (a) low and (b) high attenuation situations, respectively. In each figure part the two curves correspond to two zenith angles: (bottom) 0° and (top) 60° .

resonance region, the algorithm requires an improvement, for instance by taking ground pressure into account. A better solution would be to use a radiometer having with a third channel near 50 GHz, but in this case another algorithm would have to be developed. Rain attenuation present in the second sample (Figure 5b) is correctly estimated for zenith angles equal to zero (i.e., for a small thickness of the atmosphere). When the thickness of the rain layers increases (i.e., for higher zenith angle) and in particular for frequencies higher than

30 GHz, attenuation becomes more sensitive to the presence of rain, leading to very high attenuation (higher than 15 dB). In that case, the algorithm should not be used, except if a weak accuracy is accepted, because, as mentioned in the previous statistical study, strong underestimation are observed. The algorithm cannot be used in such cases except if a good accuracy is not required. However, for many applications in the field of telecommunications, it is very useful to have a good knowledge of attenuations in Ka-band only up to 10 dB. This

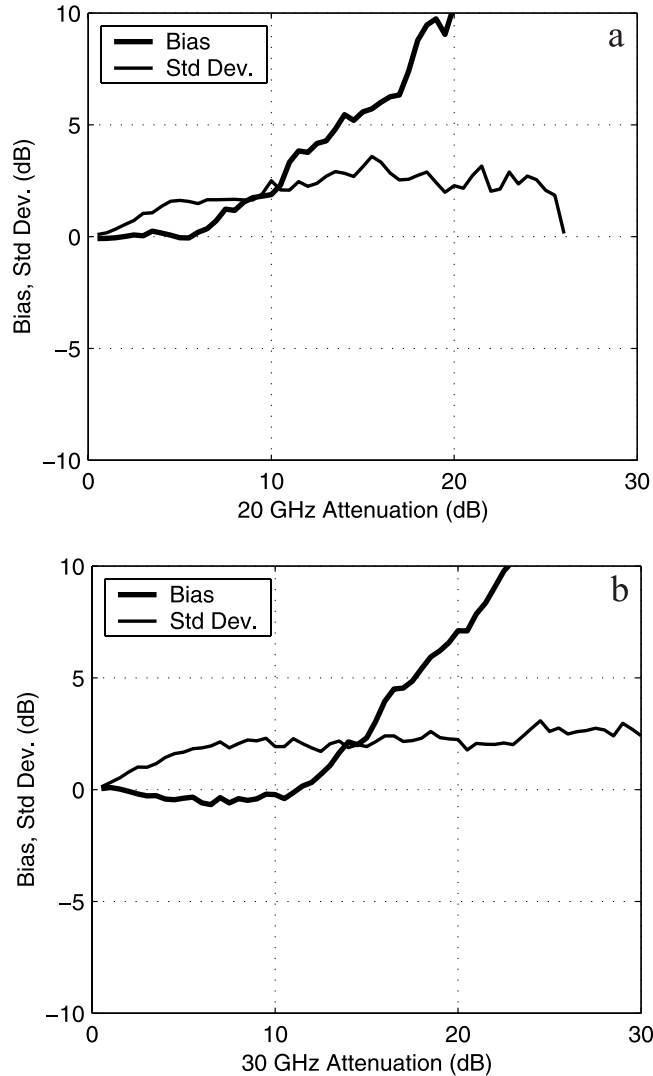


Figure 6. Generalization error of the NN attenuation model at (a) 20 and (b) 30 GHz obtained on actual data measured during the Olympus experiment. The thick line corresponds to the error bias, and the thin line corresponds to standard deviation error as a function of attenuation.

would be the case, for example, of Very small Aperture Terminals (VSAT).

5.3. Confronting the Model to Measured Data

[41] The NN attenuation model was applied to the derivation of atmospheric attenuation at different frequencies from the brightness temperatures measured by the dual-frequency radiometer RESCOM during the *Olympus Propagation Experiment (OPEX)* [1994]. For the two beacon frequencies (20 and 30 GHz), the obtained attenuations, derived from the radiometer measurements, are compared with those directly measured between the satellite and the ground station (see

Figure 6). These data have been collected during five consecutive months (May–September 1992) by the French Olympus ground station in Gometz la Ville (near Paris) for a zenith angle of 60° .

[42] With this measured data set, the algorithm gives a good agreement between beacon and radiometer attenuations, when it is smaller than 6 dB (10 dB) for 20 GHz (30 GHz). For higher attenuations an increase in bias is observed like in results presented above for simulated data (Figure 4). This is deemed as validating the NN attenuation models at 20 GHz and 30 GHz, even if scatter noted for the measured data is, of course, more significant than with simulated data.

[43] No direct validation can be performed for the other frequencies. However, the good agreement observed with the 20 and 30 GHz beacon measurements also provides an a priori validation of the databases used to develop the different algorithms. Atmospheric profiles and the radiative transfer model used being identical for all frequencies between 20 and 50 GHz, this partial validation is an evidence of the fact that the results obtained are also relevant for the other channels.

[44] Moreover, for these higher frequencies the validity range of the attenuation algorithm will increase. In fact, as explained in section 3.1 this limitation comes from the saturation phenomenon observed on measured brightness temperatures themselves. Saturation starts from a 20 GHz attenuation of 6 dB, corresponding to a 50 GHz attenuation of about 20 dB (see Figure 1).

[45] It is not easy to compare with others algorithms because they are not devoted to strong attenuations, i.e., for rainy conditions or in presence of heavy clouds. In clear-sky condition (low attenuation) the performances of our algorithm are very similar to those of other algorithms. However, our algorithm contrary to others, is not devoted to particular frequency and elevation angle, but can be used for any frequencies between 20 and 50 GHz.

6. Applications

[46] In this section some applications of this new NN attenuation model are presented.

6.1. Attenuation Statistics

[47] Our new NN attenuation model has been applied to RESCOM measurements made during the Olympus experiment. The experimental data used here were obtained between May and October 1992 in Gometz-la-Ville (France). Figure 7 shows the statistics, in time percentage, for the cumulated attenuation obtained at different frequencies. A threshold of, for example, 8 dB is reached during 0.16%, 0.41%, 0.88% and 2.15% of the time for frequencies equal to 20, 30, 40 and 50 GHz, respectively. This amounts to more than 7 days per year for the 50 GHz channel. These curves underline the difficulty encountered when using Ka or Q-band or higher frequencies for telecommunications applications.

[48] Figures 7a and 7b make it possible to compare statistics obtained at 20 and 30 GHz, on the one hand, directly using the beacons of the Olympus satellite, and on other hand, with the NN model applied to radiometer measurements. Here again, the limitation in the estimation of strong attenuations is observed. The underestimation of larger attenuations makes it difficult to use the rightmost part of these curves. However, for attenuations

lower than 10 dB a good agreement is observed with Olympus results, which is useful for most studies on communications satellite systems.

6.2. Beacon Calibration

[49] Because of the limitation of the approach previously mentioned, high atmospheric attenuation can only be determined accurately with the aid of a satellite beacon signal. Naturally, this can be done only for a particular frequency and a particular zenith angle. For future experimental satellite with Ka and Q bands beacons on board, it is important to determine the 0 dB level relative to which the atmospheric attenuation is measured. In fact, this no-attenuation level is not constant because the transmitted signal shows daily variations caused by possible satellite motions and temperatures changes. To separate daily variations of the satellite beacon signal from propagation effects, a dual-frequency radiometer is thus used to perform accurate measurements of clear-sky attenuation independently of satellite variations. The model described above in section 3.2.2, as previously pointed out has been developed in the context of the Olympus experiment to calibrate the beacon signal using the radiometer system, under clear-sky conditions, with an accuracy of more than 0.1 dB. The NN model developed in this paper is well suited to atmospheric attenuation retrieval from radiometer measurements to perform the calibration of the Ka and Q bands beacons. Considering the performance of the present model for beacons frequencies of 20.7 and 41.4 GHz (corresponding to frequencies band allocated to this kind of study) and zenith angles between 30 and 60° and for clear-sky attenuation estimation only, the error distribution shown in Figure 8 was obtained. The aim of 0.1 dB accuracy is thus always reached for the 20 GHz channel. For the 41.4 GHz channel an accuracy of 0.2 dB is reached, which is a good but required result for the study of link impairment to be performed during this coming experiment.

6.3. Satellite Diversity for Satellite Constellation

[50] In the considered frequency band, strong rain results in temporary unavailability of the radio link. However, atmospheric liquid water in clouds or rain has the property of being spatially heterogeneous, with rain cells of a few square kilometers only. Thus, using a technique known as satellite diversity can solve temporary radio link unavailability. It is clear that gains in service availability through satellite diversity would be more significant if the various links behaved in an uncorrelated manner or, if they presented low correlation values, which are more likely to occur when the angular separation between links is large. The correlation coefficient for different angular separations of links is thus

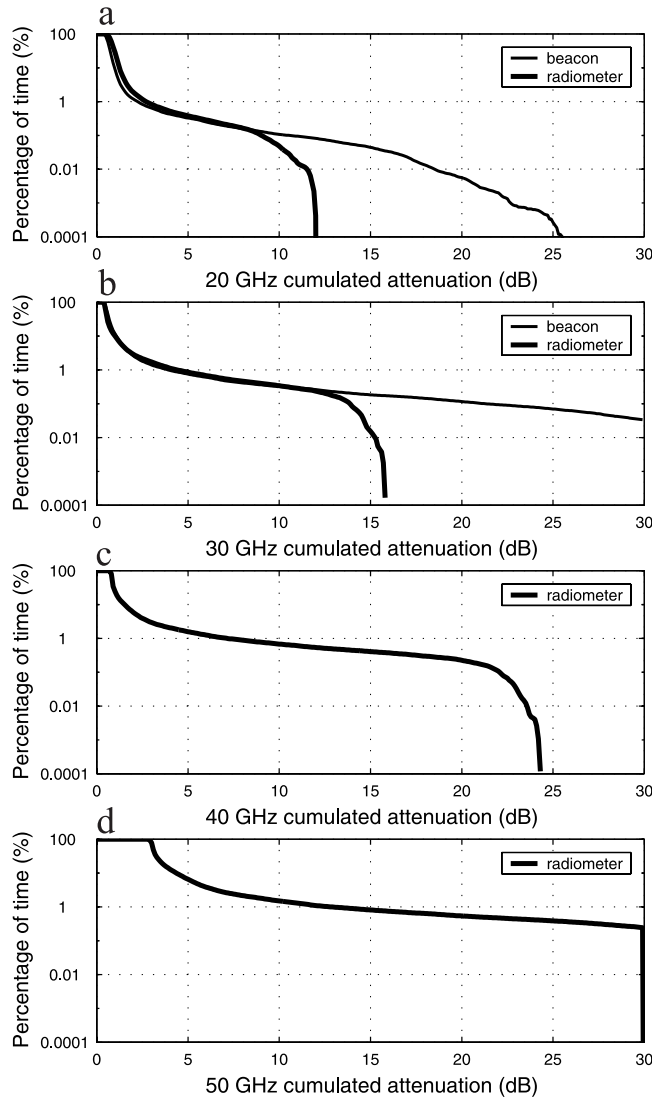


Figure 7. Exceedance time percentages of attenuation estimated by means of the Olympus beacons (thin) or deduced from radiometer measurements by means of the NN model (thick). Frequencies of (a) 20, (b) 30, (c) 40, and (d) 50 GHz are shown.

useful to evaluate the benefits of satellite diversity. In view of the quantification of this correlation, a measurement campaign is in progress, using two radiometers, as described below. Preliminary results obtained between July 2000 and February 2001 are presented in this section.

[51] Two radiometers placed side by side measure the atmospheric attenuation simultaneously for two different pointing directions. The RESCOM radiometer is a scanning radiometer that performs measurements at 23.8 and 31.7 GHz frequencies and the DRAKKAR radiometer measurements are obtained at 23.8 and

36.5 GHz. The NN model presented in this paper has been applied to these brightness temperatures to derive the atmospheric attenuation at four frequencies (20, 30, 40 and 50 GHz).

[52] Since we only want to study the effect of atmospheric heterogeneity, the attenuations used in the next paragraphs are normalized so as to make them independent of atmospheric thickness, i.e., of elevation angle. The normalized attenuation is given by

$$A_N(f, \theta) = \frac{A(f, \theta)}{\cos(\theta)}. \quad (15)$$

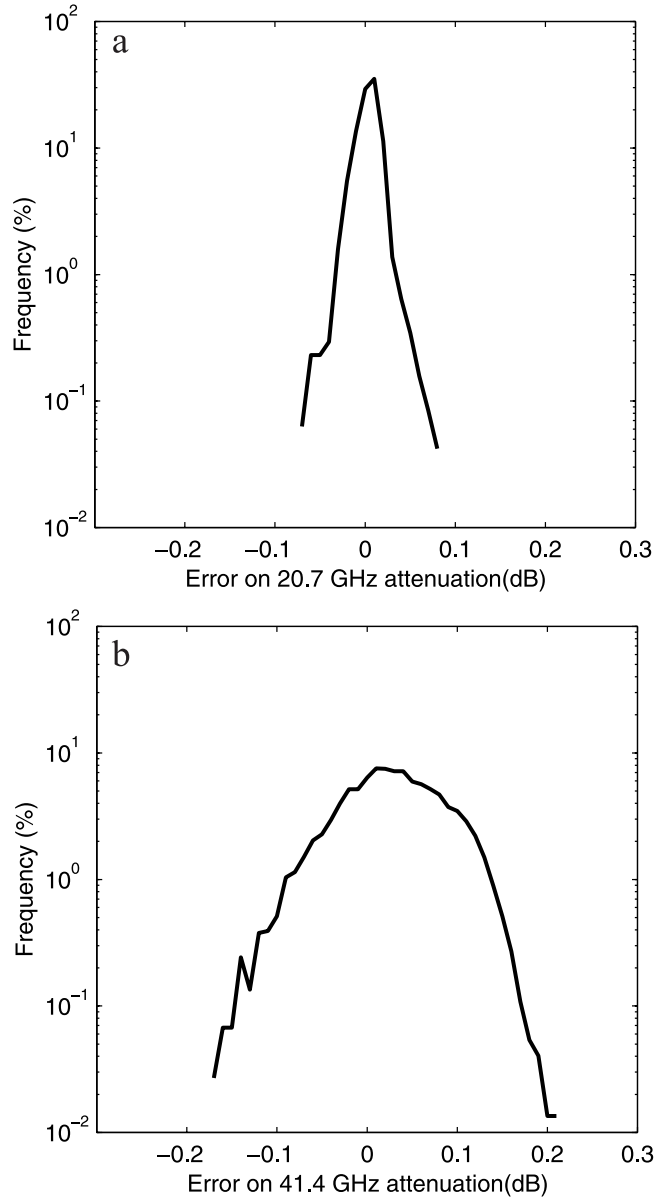


Figure 8. Distribution of the NN model error (a) on the 20.7 GHz attenuation, and (b) on the 41.4 GHz attenuation retrieved from brightness temperatures measured at 21.3 GHz and 31.6 GHz.

With normalized attenuation, the differences observed between two directions can be attributed mainly to spatial heterogeneity of rain or clouds.

6.3.1. Case Study

[53] Figure 9 shows for a particular event the interest of satellite diversity in case of inhomogeneous atmosphere. 40 GHz attenuations estimated from DRAKKAR measurements in the zenith direction are plotted on the x axis, and 40 GHz normalized attenuations estimated from RESCOM simultaneous measurements at a zenith

angle of 60° in the west direction are plotted on the y axis. These measurements are obtained at the beginning of a rain event and thus correspond to a period of increasing attenuation. At the beginning, the atmosphere is homogeneous and the two normalized attenuations are equal to 0.5 dB. When the rain cell approaches the experimental site, the attenuation estimated on the slant path increases abruptly, whereas the attenuation measured in the vertical direction remains constant. Little by little, the precipitating cell moves on, and the vertical path also becomes

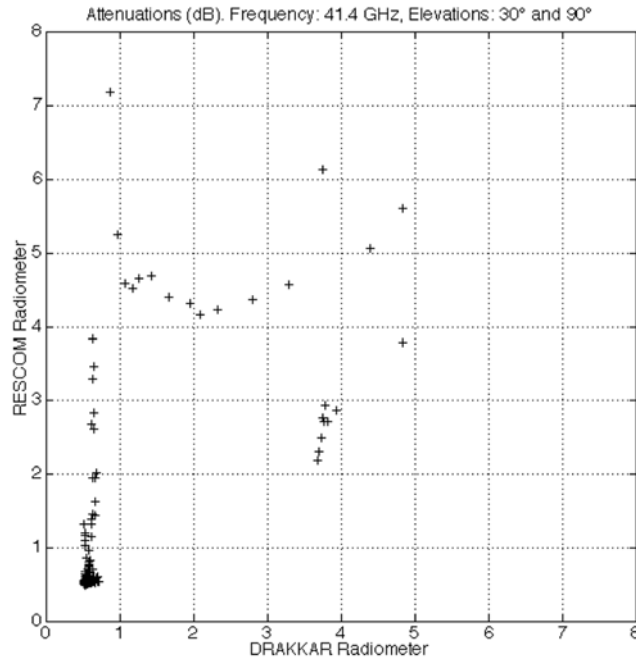


Figure 9. Evolution of the 40 GHz attenuation at two pointing directions: The zenith attenuation is shown on the x axis, and the attenuation measured for a 60° zenith angle towards the west is shown on the y axis.

affected by strong attenuation. The end of this event could not be represented because a water layer was present on the radiometer reflector, was not too thick to be removed by the blower system. This typical case shows how satellite diversity can increase the quality of the link.

6.3.2. Statistical Study

[54] Joint statistics between atmospheric attenuations measured in various pointing directions are presented in Figure 10 for the 40 GHz channel. These statistics are obtained for two paths in the east/west directions. The four different subplots corresponds to $\theta_1 = 5^\circ, 18^\circ, 23^\circ$ and 41° . For each pair of angles ($\theta_2 = -\theta_1$) the correlation coefficient $\rho(\theta_1, \theta_2)$ is given. When the distance between the two paths increases the effect of heterogeneity also increases, which explains the increased scattering around the bisecting line. For an angular separation between paths increasing from 10° to 82° the correlation coefficient ρ decreases from 0.98 to 0.8.

[55] Figure 11 shows, for the four considered frequencies, the improvement in terms of the exceedance time percentage of the attenuation brought about by satellite diversity. Statistics of cumulated attenuation obtained in one pointing direction are compared with those obtained when a second pointing direction is simultaneously available. In this second case, a “diversity attenuation” is defined as the smaller of the two attenuations obtained

on the two directions. The attenuation considered alone corresponds to a path with a hypothetical satellite located towards the west. The technique of satellite diversity is applied in the case when two hypothetical satellites are simultaneously visible towards the west and the east. The two ground-satellite paths have a zenith angle of 40° .

[56] Results obtained for this particular configuration showed a significant improvement in service availability thanks to the diversity effect. At 20 GHz (30 and 40 GHz, respectively) with only one satellite, the attenuation is greater than 7 dB (16 and 30 dB, respectively) during 0.01% of time, whereas it is brought back to 4 dB (8.5 and 16 dB, respectively) if the two satellites are judiciously used, that is, if the less attenuated path is always used. The statistics computed here show that the mean attenuation at 0.01% of time with two satellites ($A_2^{0.01\%}$) is related to the one obtained with one satellite only ($A_1^{0.01\%}$) by the following law:

$$A_2^{0.01\%} = r(\theta) A_1^{0.01\%} \quad \text{with} \quad \begin{cases} r(40^\circ) = 0.56 \\ r(16^\circ) = 0.66 \\ r(10^\circ) = 0.96 \\ r(0^\circ) = 1. \end{cases} \quad (16)$$

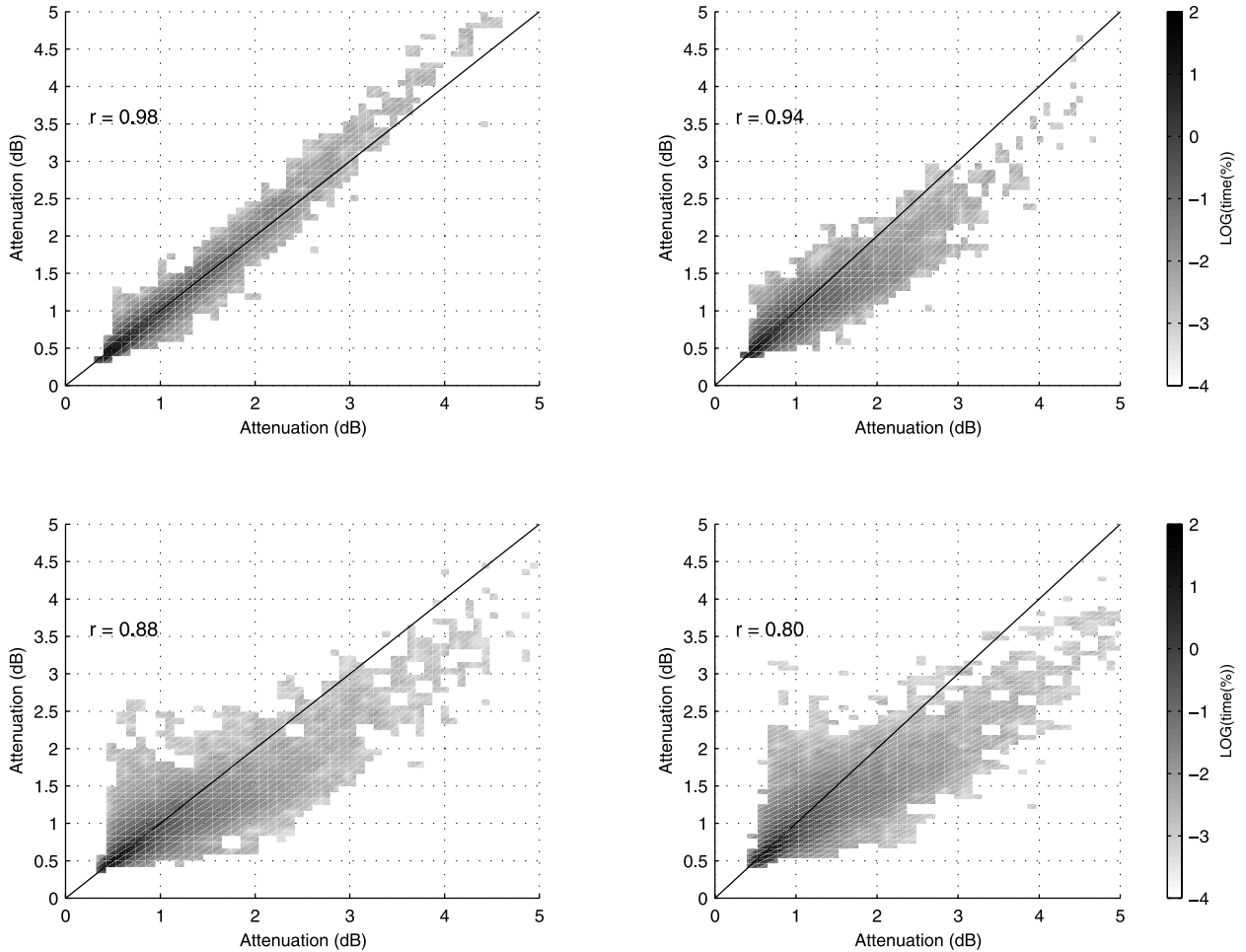


Figure 10. Joint statistics between atmospheric attenuation observed for four different pairs of angles $(\theta_1, -\theta_1)$ at 40 GHz. The corresponding correlation coefficients are given. Angle pairs, from left to right, and top to bottom: $5^\circ, 18^\circ, 23^\circ, 41^\circ$. See color version of this figure at back of this issue.

The variation of coefficient $r(\theta)$ is relatively independent of frequency with a variation of less than 5% for frequencies between 20 and 50 GHz.

[57] When the zenith angle θ decreases, $r(\theta)$ tends towards 1. As could be expected, for θ equal to 0, both paths are identical. This diversity coefficient is related to atmospheric heterogeneity, so that it increases when the path separation decreases (that is for increasing θ). Only partial results are presented here to show the applications of the present NN model, but satellite diversity is a wide subject that would need a more in-depth study, which is outside the scope of the present work.

7. Conclusion

[58] A large and statistically representative simulated database allows a NN attenuation model to be developed.

This model estimates the atmospheric attenuation for frequencies between 20 and 50 GHz from dual-beam radiometer data for any pointing direction. The optimal model is a MLP with four inputs (brightness temperatures measured at frequencies near 22.5 and 30 GHz, the cosecant of the zenith angle and frequency), two hidden layers with 18 neurons each and one output (the atmospheric transmissivity).

[59] This statistical model has been successfully validated for the 20 and 30 GHz channels through a comparison between the modeled atmospheric attenuation derived from radiometer measurements and attenuation directly measured on satellite beacons (Olympus).

[60] Under clear-sky conditions, this new model gives an accuracy better than 0.1 dB at 20 GHz and better than 0.2 dB at 41 GHz. It can thus be used for satellite beacon calibration in Ka or Q bands. For other atmospheric

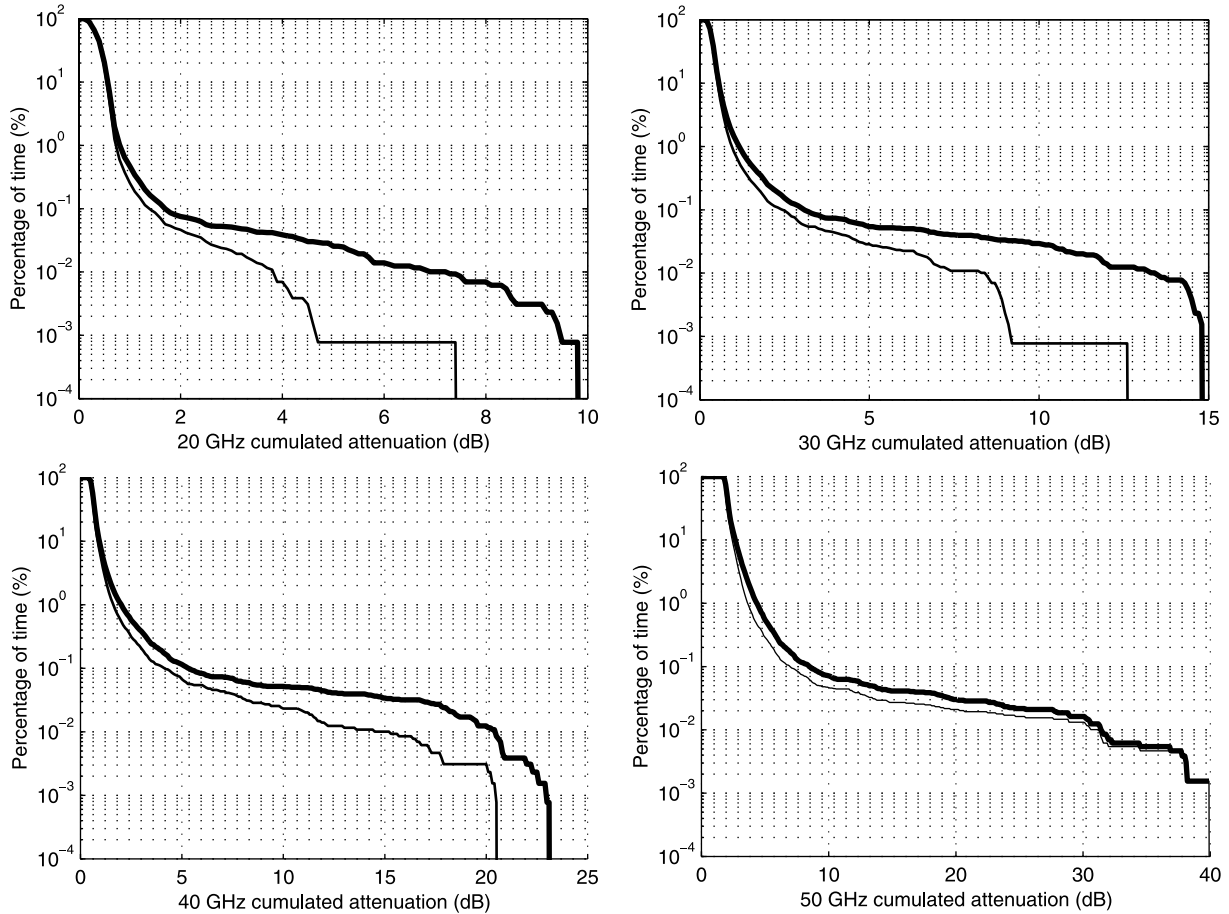


Figure 11. Exceedance time percentage of attenuation at 20, 30, 40 and 50 GHz with only one visible satellite (thick line), and with two simultaneously visible satellites (thin line).

conditions (clouds or rain), the validity range of this new model is much wider than other existing models.

[61] This new model, when applied to radiometer measurements, will allow the simultaneous study of one or several links, and thus make it possible to take attenuation correlation effects into account. This approach can be used to use correlation coefficient data as inputs to statistical propagation models for evaluating diversity gain.

[62] The preliminary statistical results obtained at 40 GHz shows the interest of satellite diversity, with a diversity gain ranging from 1 to 0.56 for zenith angles from 0° to 40° .

[63] The model presented in this study is available in MATLAB[®] on direct request from the authors.

References

- Arbesser-Rastburg, B., Propagation issues for present and future satellite systems, paper presented at 4èmes Journées d'études: Propagation Electromagnétique dans l'Atmosphère du Décimétrique à l'Angström, Univ. de Rennes 1, Rennes, France, March 2002.
- Bishop, C. M., *Neural Networks for Pattern Recognition*, Oxford Univ. Press, New York, 1995.
- Bosisio, A. V., and C. Mallet, Influence of cloud temperature on brightness temperature and consequences for water retrieval, *Radio Sci.*, 33(4), 929–939, 1998.
- Chandrasekhar, S., *Radiative Transfer*, Dover, Mineola, N. Y., 1960.
- Cibenko, G., Approximation by superpositions of a sigmoidal function, *Math. Control Signals Syst.*, 2, 303–314, 1989.
- English, S. J., C. Guillou, C. Prigent, and D. C. Jones, Aircraft measurements of water vapour continuum absorption at millimeter wavelengths, *Q. J. R. Meteorol. Soc.*, 120, 603–625, 1994.
- Gérard, E., and L. Eymard, Remote sensing of integrated cloud liquid water: Development of algorithms and quality control, *Radio Sci.*, 33, 433–447, 1998.

- Haykin, S., *Neural Networks: A Comprehensive Foundation*, Prentice-Hall, Old Tappan, N. J., 1999.
- Hornik, K., M. Stinchcom, and H. White, Multi-layered feed-forward networks are universal approximators, *Neural Networks*, 2, 359–366, 1989.
- Kohonen, T., *Self Organizing Maps*, Springer-Verlag, New York, 2001.
- Liebe, H. J., G. A. Hufford, and M. G. Cotton, Propagation modeling of moist air and suspended water/ice particles below 1000 Ghz, paper presented at 52nd Specialists Meeting of Electromagnetic Wave Propagation, Adv. Group for Aerosp. Res. and Dev., Brussels, Belgium, 1993.
- Mallet, C., and J. Lavergnat, Beacon calibration with a multi-frequency radiometer, *Radio Sci.*, 27(5), 661–680, 1992.
- Marshall, J. S., and W. M. K. Palmer, The distribution of rain drops with size, *J. Meteorol.*, 5, 165–166, 1948.
- Moreau, E., C. Mallet, and C. Klapisz, Effects of aspherical ice and liquid hydrometeors on microwave brightness temperatures, in *Microwave Radiometry and Remote Sensing of the Earth's Surface and Atmosphere*, edited by P. Pampaloni and S. Paloscia, pp. 291–298, VSP, Zeist, Netherlands, 1999.
- Olympus Propagation Experiment (OPEX), Reference book on Radiometry and Meteorological Measurement - Reference book on Attenuation Measurement and Prediction, *ESA WPP-083*, 1994.
- Polonio, R., and C. Riva, ITALSAT Propagation Experiment at 18.7, 39.6, and 49.5 GHz at Spino d'Adda: Three years of CPA statistics, *IEEE Trans. Antennas Propag.*, 46(5), 1998.
- Rosenkranz, P. W., Water vapor microwave continuum absorption: A comparison of measurements and models, *Radio Sci.*, 33(4), 919–928, 1998.
- Tiedtke, M., Representation of clouds in large-scale models, *Mon. Weather Rev.*, 121, 3040–3061, 1993.
- Tsang, L., J. A. Kong, and R. T. Shin, *Theory of Microwave Remote Sensing*, John Wiley, Hoboken, N. J., 1985.
- Ulaby, F. T., R. K. Moore, and A. K. Fung, *Microwave Remote Sensing: Active and Passive*, vol. 1, *Microwave Remote Sensing Fundamentals and Radiometry*, Artech House, Norwood, Mass., 1981.
-
- L. Barthes, P. Gole, and C. Mallet, Centre d'Etude des Environnements Terrestres et Planétaires (CETP), 10–12 avenue de l'Europe, 78140 Vélizy, France. (barthes@cetp.ipsl.fr; gole@cetp.ipsl.fr; mallet@cetp.ipsl.fr)

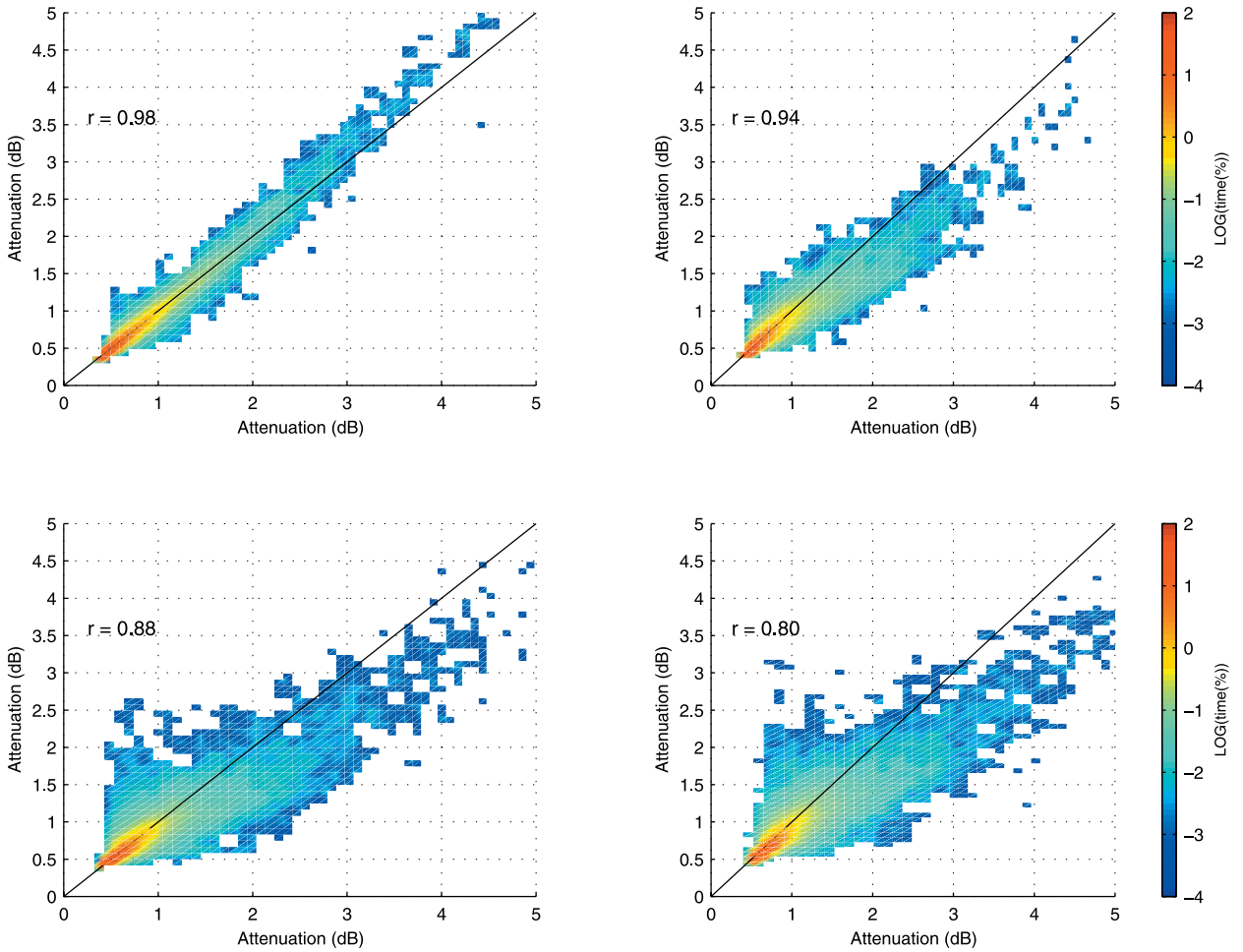


Figure 10. Joint statistics between atmospheric attenuation observed for four different pairs of angles $(\theta_1, -\theta_1)$ at 40 GHz. The corresponding correlation coefficients are given. Angle pairs, from left to right, and top to bottom: 5° , 18° , 23° , 41° .